A Thermally Actuated Fully Inkjet-Printed Origami-Inspired Multilayer Frequency Selective Surface With Continuous-Range Tunability Using Polyester-Based Substrates

Syed Abdullah Nauroze, *Student Member, IEEE*, and Manos M. Tentzeris, *Fellow, IEEE*

***Abstract*— A first-of-its-kind design methodology to realize thermally actuated origami-inspired multilayer Miura frequency selective surfaces (MLM-FSSs) using a polyester-based substrate is presented in this article that can change its frequency response according to the variation in its ambient temperature. In order to maintain the optimum interlayer distance between the two-layer Miura-FSS structures, a specialized low-loss origami-inspired spacer layer is introduced that preserves its desired overall frequency response during different folding configurations. It also features an unprecedented high mechanical strength, making it suitable for a wide range of terrestrial, outer-space, and biomedical applications. The frequency response and its relationship to kinematics of the proposed structure are also presented in detail, which gives a unique insight into the operation principles of such structures. The proposed structure features twice the bandwidth as compared to single-layer Miura-FSS, an excellent angle of incidence rejection, and is the first demonstration of a fully inkjet-printed MLM-FSS that is realized completely by a rigid heat-sensitive substrate as opposed to traditional cellulose-based Miura-FSSs that lack self-actuation mechanism as well as rigidity, which is a key attribute of most practical thick origami structures.**

***Index Terms*— Inkjet-printing, Miura, multilayer frequency selective surface (FSS), origami, tunable filters.**

I. Introduction

FREQUENCY selective surfaces (FSSs) are spatial filters that reflect, transmit, or absorb specific bands of incident electromagnetic (EM) waves and typically consist of a 2-D or 3-D periodic array of resonant elements on a thin substrate. The frequency response of an FSS is primarily determined by the size, shape, and type of the resonant element along with their interelement distances. These structures have found many applications, including radomes, reflectors, transmitarrays, and reducing antenna radar cross section [1], [2].

Traditional FSS structures are unable to change their frequency response which limits their use in real-life applications. One of the most popular tuning mechanism for these structures includes changing the electrical properties of the resonant elements by using electronic components, such as varactors, p-i-n diodes, and microelectromechanical switches (MEMSs) [3]–[6]. Other methods include the use of ferrite-based substrates or the integration of microfluidics within the substrate to vary its effective permittivity by biasing it with a dc magnetic field or with different filling liquids, respectively [7]–[9]. While electrically tunable RF structures can realize a fast EM response reconfigurability, they are laborious, expensive, and require continuous high operational voltages. They also suffer from high rates of failure and limited tunability range, which makes them impractical as the overall size of the structure increases. On the other hand, ferrite- or microfluidics-based techniques also require high operational voltages and are hard to control. That is why mechanical tuning mechanisms are gaining popularity due to their superior power handing capability, quality factor, linearity, and wide-band (continuous range) tunability. However, their bulky size, heavy weight, and low switching/tuning speed have restricted their use in modern communication systems.

Recently, origami-inspired single-layer Miura FSS (SLM-FSS) structures have been proposed that facilitate wide-range tunability by simply changing their physical shape to effectively vary the electrical length of resonators and/or their interelement coupling [10]–[12]. While these structures facilitate high power handling capability similar to the mechanically tuned RF structures, they also suffer from slow tuning capability. However, their fabrication complexity is significantly lower as compared to traditional mechanically tuned RF structures or fully 3-D printed RF structures because it involves first inkjet-printing conductive traces on a 2-D surface and then folds it to realize any complex 3-D structure. SLM-FSS structures require a single degree of actuation, which greatly simplifies tuning mechanism as compared to traditional mechanically tuned RF structures. Moreover, they are lightweight structures that feature relatively higher

Manuscript received May 3, 2019; revised August 20, 2019; accepted September 15, 2019. Date of publication November 1, 2019; date of current version December 27, 2019. This work was supported in part by the NSF, the U.S. Department of Defense Threat Reduction Agency, and Semiconductor Research Corporation, under Grant RD928, Grant RE202, and Grant RG460, in part by the Air Force Office of Scientific Research under Grant FA9550-18-1-0191, and in part by the Georgia Tech Institute for Electronics and Nanotechnology, a member of the National Nanotechnology Coordinated Infrastructure (NNCI), which is supported by the National Science Foundation, under Grant ECCS-1542174. This article is an expanded version from the IEEE MTT-S International Microwave Symposium (IMS 2019), Boston, MA, USA, June 2–7, 2019. *(Corresponding author: Syed Abdullah Nauroze.)*

The authors are with the School of Electrical and Computer Engineering, Georgia Institute of Technology, Atlanta, GA 30332 USA (e-mail: nauroze@gatech.edu).

Color versions of one or more of the figures in this article are available online at http://ieeexplore.ieee.org.

Digital Object Identifier 10.1109/TMTT.2019.2946074

mechanical strength (as compared to traditional 2-D FSS structures) and facilitate on-demand deployability. These features make them a good candidate for outer space and biomedical applications that have limited external power sources for tuning as well as require large structures to be stowed in a small volume that can be deployed on-demand to full scale at the destination [13]. Some of the key applications for this technology include deployable reflectarrays for cubesates, reconfigurable radomes, miniaturized high gain antennas, shielded walls, and large intelligent surfaces for 6G [14]–[18].

Traditional SLM-FSS and multilayer Miura-FSS (MLM-FSS) structures were realized using cellulose-based substrates that are good for proof-of-concept purposes but have limited practical applications [10], [15]. This is due to the fact that these substrates are prone to absorb moisture, feature high dielectric losses, and require up to ten layers of conductive ink with 2 h, curing time to achieve good conductivity values. They also require mechanical actuation mechanisms to reconfigure their physical shape, making them unsuitable for outer space and biomedical applications where total available power is limited. Traditional SLM-FSS structures can only realize limited tunability range and bandwidth that can be improved by meander-line configurations [12]. Finally, an SLM structure with nonrigid facets tends to curl up when folded, thereby changing the designated frequency response of the FSS structure [15]. These problems can be mitigated by using MLM-FSS configurations, but the realization of a shape-reconfigurable spacer layer between the SLM-FSS structures that can change the interlayer distance according to the variation in frequency response of each SLM-FSS is challenging. Recently, inline and mirror MLM-FSS configurations consisting of two SLM-FSS structures joined together at the valley foldlines have been proposed in [15]. However, these structures neither support adding more than two SLM-FSS layers nor do they maintain a given frequency response with different folding states. These problems are addressed by a novel MLM-FSS structure with a thermally actuated spacer layer in [19], but a key disadvantage of the structure is that it can only realize limited actuation even at high temperatures due to the use of cellulose-based SLM-FSS layers.

The rest of this article is organized as follows. First, a new heat-sensitive polyester-based substrate is introduced in Section II for the realization of self-actuating origami-based RF structures. Next, the MLM-FSS structure along with an in-depth description of its fabrication, actuation mechanism, and kinematics analysis is presented in Section III. A comprehensive discussion regarding simulation and measurement results along with an equivalent circuit model (ECM) of the proposed MLM-FSS structure is presented in Section IV, and finally, the conclusions are given in Section V.

II. Polyester Versus Cellulose-Based Substrate for Origami Structures

Traditional origami-inspired FSS structures use cellulose substrates [10]–[12], because they facilitate the realization of highly flexible conductive traces and are easy to fold manually.

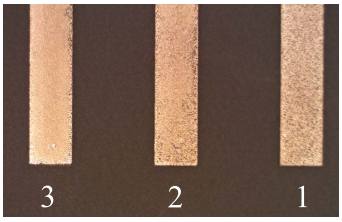

Fig. 1. Inkjet-printed conductive traces with different numbers of SNP ink layers on the polyester-based substrate.

However, these structures have found limited applications, as they require mechanical actuation mechanisms that considerably increase the power requirements and complexity of the overall system. High porosity and dielectric losses of these substrates also restrict their use in high-frequency applications. For example, due to the high porosity of the cellulose substrates, it is very difficult to achieve conductive traces with high resolution, as the silver nanoparticle (SNP) ink tends to spread into the substrate during the inkjet-printing process. Furthermore, the realization of highly conductive traces requires inkjet printing of at least ten layers of SNP ink and sintering for a minimum of 2 h at 150 °C, which significantly increases the overall fabrication time [20]. It is also important to note here that using a large number of SNP ink layers on a porous cellulose substrate also makes slot-like RF structures hard to realize, as these substrates tend to bend and buckle when wet, resulting in an uneven surface. However, this effect is not pronounced for conductive traces and dipole-like structures.

In order to address these challenges, a low-loss, heat-sensitive 90-μm-thick polyester-based substrate film ($\epsilon_r = 2.92$ and $\tan\delta = 0.0088$ at 8 GHz) is used in this article that transitions from rigid to soft/flexible state when heated. It is also hydrophobic in nature that allows most of the SNP ink to be deposited on the substrate surface during the inkjet-printing process, thereby facilitating the realization of the conductive traces with higher resolution and conductivity values while utilizing a significantly lower number of SNP layers and curing time as compared to cellulose substrates.

Micrographs of inkjet-printed (2-mm wide and 20-mm long) conductive traces on a polyester-based substrate for different numbers of layers of SNP ink (SunChemical EMD-5730) are shown in Fig. 1. The traces were cured at 150 °C for 15 min in an oven to evaporate the ethanol solvent and improve their overall conductivity. It was observed that trace resistance decreases slightly going from two (0.04 $\Omega/\square$) to three (0.03 $\Omega/\square$) layers of SNP ink but remained constant for higher numbers of layers. Therefore, only two layers of SNP ink were used in this article to realize inkjet-printed conductive traces to save fabrication time and more importantly improve overall flexibility of the trace. This is due to the fact that conductive ink on the surface of a hydrophobic substrate typically becomes relatively inflexible after the sintering process; therefore, a higher number of inkjet-printed layers increase the probably peeling off during bending process. This problem can be circumvented by using a lower number of SNP layers or using specialized "bridge-like" structures at sharp bends/foldlines of the origami structure [10].

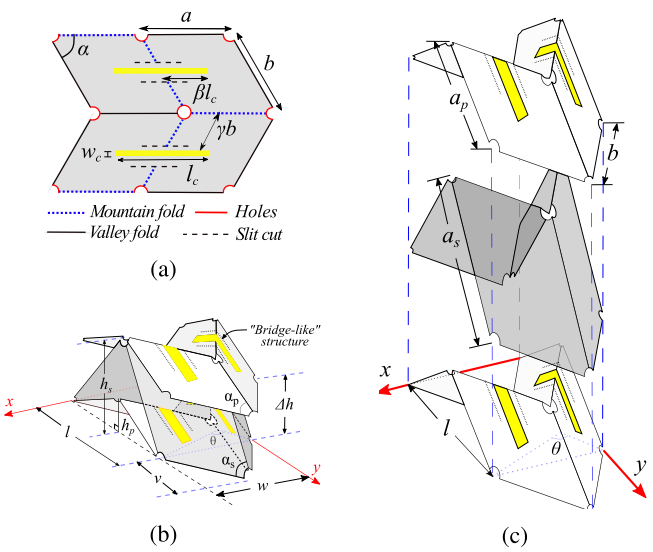

Fig. 2. (a) Unit cell of an SLM-FSS in flat configuration ($\theta = 180°$). (b) Unit cell of MLM-FSS in folded configuration ($\alpha_p = 45°$). (c) Exploded view of the MLM-FSS with $b_s = b_p = b = a_p = 20$ mm. $\beta = \gamma = 0.5$, $l_c = 20$ mm, and $w_c = 2$ mm.

The rigid-to-soft phase transitioning property of the polyester-based substrate can be used to unfold an origami structure making it useful for the realization of real-time deployable RF structures. This is in contrast to cellulose-based substrates that need to be folded and unfolded mechanically. On the other hand, the polyester-based structures are relatively difficult to fold, tend to crack when bent or folded at sharp angles in their rigid state, and are challenging to perforate using common blade-based perforation machines as compared to the cellulose substrates. Therefore, a low-power laser was used in this article to perforate the required origami (Miura) pattern with a perforation size optimized such that the substrate does not crack at the foldlines. Moreover, holes were etched at each central vertex of the Miura pattern to avoid crack propagation [21] and make the folding process easier.

III. Thermally Actuated Dipole-Based MLM-FSS Structures

The unit cell of Miura-Ori tessellation consists of four parallelograms (each with lengths a and b and an internal angle α) connected to each other along the edges to form the foldlines, as shown in Fig. 2(a). The foldlines either curve up (mountain fold) or curve down (valley fold) as the Miura structure is folded, depicted by the change in dihedral angle θ or equivalently lengths w or l that are related to each other in [10]

$$\begin{aligned} l &= 2a\zeta \\ h &= a\zeta \tan\alpha \cos(\theta/2) \\ w &= 2b\xi \\ v &= b(1-\xi^2)^{1/2} \end{aligned} \tag{1}$$

where

$$\begin{aligned} \zeta &= \cos\alpha(1-\xi^2)^{-1/2} \\ \xi &= \sin\alpha \sin(\theta/2). \end{aligned}$$

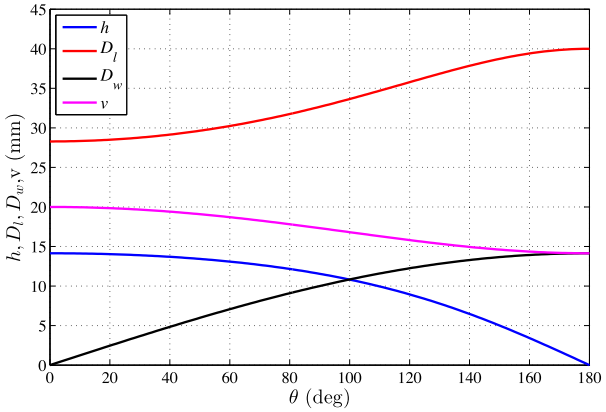

Fig. 3. Variation of key design parameters of the SLM-FSS structure with respect to folding angle θ ($\alpha_p = 45°$).

Typical SLM FSS structures are realized by inkjet-printing dipoles across the mountain foldlines of Miura-Ori tessellation, as shown in Fig. 2(a). Since the dipoles are inkjet-printed on the mountain folds, the electrical length and interelement distances between the dipoles systematically decrease as θ varies from 180° (flat configuration) to 0° (completely folded configuration) [10], [22]. The interelement distances along the x-axis (D_w) and y-axis (D_l) can be mathematically expressed as [15]

$$\begin{aligned} D_l &= l \\ D_w &= \gamma\, w \end{aligned} \tag{2}$$

where γ is the SLM-FSS design parameter that depicts the position of the dipole element on the Miura unit cell along the x-axis, as shown in Fig. 2(a). Variation of different parameters of a proof-of-concept SLM-FSS structure ($\alpha_p = 45°$) with respect to the folding angle is shown in Fig. 3.

The electrical length of the dipole decreases with θ due to its shape transformation from a 2-D (flat) to a (3-D) inverted V-shaped dipole configuration, which results in overall frequency response of the SLM-FSS structure to shifting to higher values. These SLM-FSS structures behave like the first-order bandstop filters with moderate frequency tunability (up to 15%) and bandwidth (10%) [10], which limits their use in real-life applications. Higher order tunable bandstop Miura-FSS filters with larger bandwidth can be easily realized using multilayer configuration with optimum interlayer distances.

Conventional multilayer FSS structures consist of two or more FSSs that are separated by a distance Δh using either special mechanical support or thick dielectric. Since interlayer distance controls the EM coupling between the FSS layers, it must change proportionally with respect to the frequency response of FSS layers such that the overall EM behavior of the multilayer FSS structure is preserved. While this is typically challenging to address for conventional multilayer tunable FSS structures, it can be easily realized for MLM-FSS structures by using specialized Miura-based spacers between the Miura-FSS layers [15], [19]. The unit cell for the MLM-FSS structure using a polyester-based substrate with inline stacking configuration (i.e., all Miura patterns have

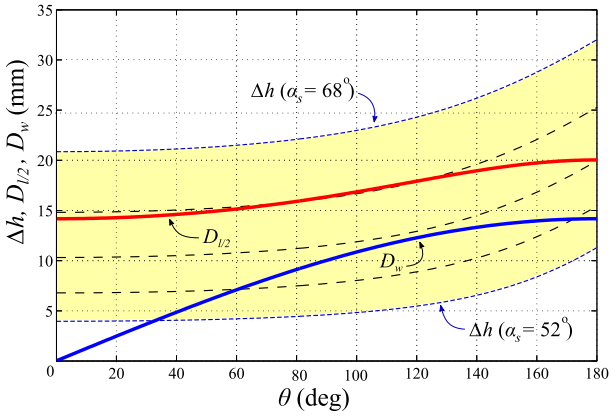

Fig. 4. Variation of key design parameters of the MLM-FSS structure with respect to folding angle θ ($\alpha_p = 45°$).

the same orientation) featuring a specialized spacer layer is shown in Fig. 2(b) and (c). Note that small (2.5-mm wide) holes were etched at all vertices to avoid crack propagation and simplify folding process. Although the design principles presented in this article are demonstrated for origami structures using thin substrates, they can be easily applied for thick origami structures using conventional or 3-D-printed flexible substrates [23].

In order to maintain the in-plane kinematics of the proposed MLM-FSS structure, all Miura layers must have the same w, l, and v values with only one independent dimension h, thereby facilitating the interlayer distance (Δh) to vary proportionally with different folding configurations. These conditions can be met by using the following design constraints:

$$a_s = a_p \frac{\cos(\alpha_p)}{\cos(\alpha_s)} \quad b_s = b_p = b \tag{3}$$

where the subscripts p and s represent the design parameters of the Miura structure with printed dipoles and spacer Miura, respectively. Since the proposed MLM-FSS configuration preserves the in-line kinematics of the overall structure, they can be completely described by the folding angle θ. The interlayer distance (Δh) can be calculated by first calculating h for the two layers using (1) and then taking the difference between them. A proof-of-concept variation of the different design parameters of the proposed MLM-FSS structure with respect to the folding angle is shown in Fig. 4.

A. Fabrication Process

The fabrication process for the proposed MLM-FSS with in-line stacking configuration is shown in Fig. 5. The two identical SLM-FSSs and the Miura-based spacer layer were realized by first perforating the Miura pattern on 90-μm-thick polyester base film using a low-power laser. The perforation size was optimized (to a size of 0.1-mm wide, 2-mm long with a spacing of 1.5 mm) to avoid any substrate cracking or breakage at the foldlines during the folding process. Moreover, a 0.2-mm wide and 8-mm long slit size was used to form "bridge-like" structures for the SLM-FSS structures that facilitate dipoles to fold in a smooth curved fashion along the foldlines rather than a sharp edge to avoid cracking or peeling off of the conductive trace, as the Miura is folded [10], [22]. These slits are not required for the spacer layer. Next, the dipoles were inkjet-printed using two layers of SNP ink and sintered at 150 °C for 15 min to increase conductivity. The resultant dipoles were highly flexible and maintained good conductivity values during bending or folding process due to the usage of a low number of SNP ink layers as well as the integration of the "bridge-like" structures that further improved flexibility by avoiding sharp folding of the dipoles.

The two SLM-FSSs and the spacer layer were then folded manually and stacked in an in-line configuration, such that the valley foldlines of the bottom SLM-FSS and the mountain foldlines of the top SLM-FSS touch the valley and the mountain foldlines of the spacer layer, respectively, while keeping the same orientation of all three Miura layers. Finally, all layers were joined together by applying heat resistant glue on foldlines of the spacer layer. The fabricated MLM-FSS structure is shown in Fig. 6 and the behavior of the inkjet-printed dipole elements on "bridge-like" structures at different folding angles is shown in Fig. 7. The introduction of holes at the vertices greatly simplifies the folding process while simultaneously making the overall Miura structure more flexible—a technique which is particularly useful for thick or 3-D printed origami structures [24]. Note that these holes do not affect the overall kinematics or the EM response of the Miura-FSS.

B. Thermal Response and Actuation Mechanism

The heat-sensitive substrate used to realize the proposed MLM-FSS facilitates actuation of the overall structure, making it an attractive candidate for terrestrial, outer-space, and EM cloaking applications, where the frequency response can be changed on-demand by simply varying the folding angle (increasing temperature). The Miura geometry also facilitates the perfect alignment of multiple FSS layers by simply stacking them along the valley foldlines, as shown in Fig. 2(b) and (c), thereby mitigating alignment errors during assembly.

In contrast to traditional Miura-FSS structures, the proposed MLM-FSS structure facilitates an integrated mechanism to change its folding behavior in response to an external stimuli (temperature) rather than a mechanical actuation. Some of the key advantages of thermally activated origami structures are their ease of use as compared to other environmental-stimuli responsive actuation mechanisms (such as light, chemical reaction, and so on) and are of particular interest in circumstances where surplus heat is readily available in the form of structure phase transition or joule heating [25]. The main drawback is that it is very hard to control precise temperature conditions to reach a specific folding configuration. This can be easily circumvented by using conductive article, graphene, or 3-D printed photothermal substrates [25]–[27]. However, heat-sensitive polyester-based substrate is used in this article to simplify actuation mechanism and fabrication process in order to extensively evaluate the EM response of MLM-FSS structures in terms of

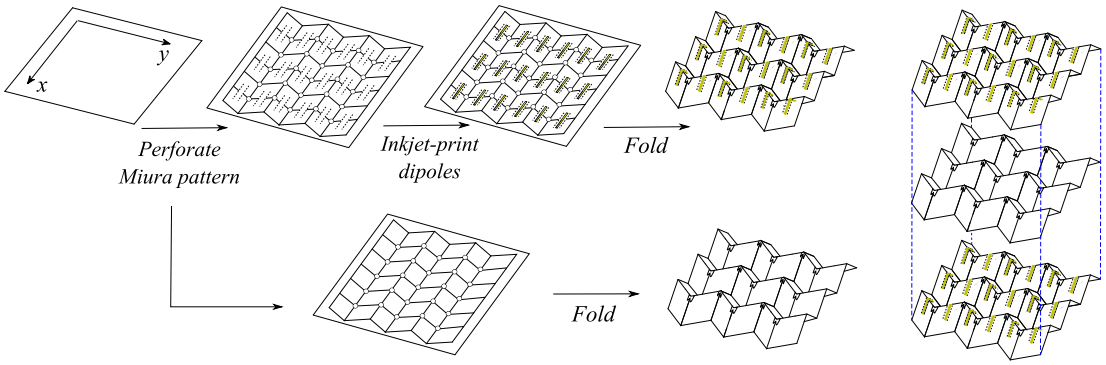

Fig. 5. Fabrication process for the realization of MLM-FSS structures.

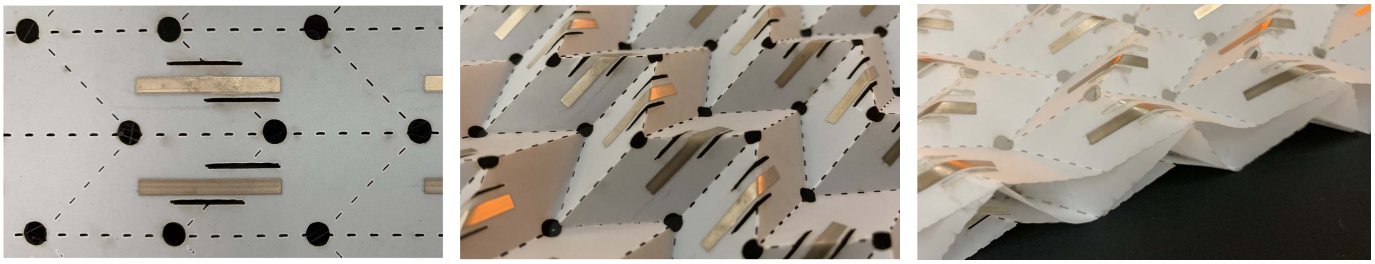

Fig. 6. Fabricated SLM-FSS in (a) flat and (b) folded configuration. (c) Complete MLM-FSS structure in folded state assembled using in-line stacking configuration.

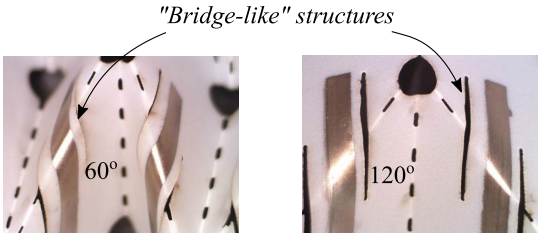

Fig. 7. Closeup of dipoles on "bridge-like" structures for different folding states (θ values).

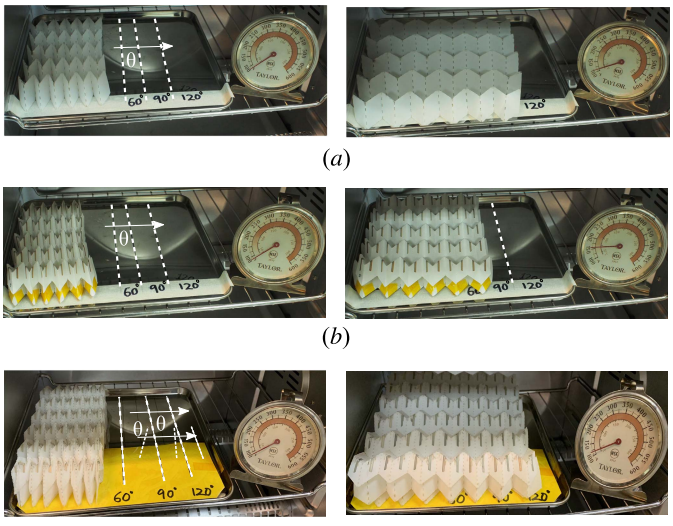

Fig. 8. Thermal actuation of (a) single-layer polyester film-based Miura structure (spacer) and MLM-FSS structure with spacer layer sandwiched between two (b) cellulose and (c) polyester-based SLM-FSS structures. The marking indicates Miura extension for different values of θ.

on-demand frequency response tunability, mechanical strength, and actuation complexity.

To demonstrate the superior performance of the MLM-FSS using only polyester-based substrates, three different samples were fabricated. These include an SLM-based spacer using the polyester-based substrate, an MLM-FSS with top and bottom SLM-FSSs realized using a cellulose-based substrate and a Miura-inspired spacer layer using the polyester-based substrate, and finally, an MLM-FSS with all three (top, spacer, and bottom) layers realized using only a polyester-based substrate. The samples were completely folded ($\theta < 60°$) and placed in an oven. Next, the oven temperature was increased gradually resulting in the unfolding of the three structures, as shown in Fig. 8. It can be easily seen that while complete polyester-based Miura structures [see Fig. 8(a) and (c)] can unfold to a larger extent ($\theta > 120°$) at moderate temperatures (~50 °C), the MLM-FSS with the cellulose substrate does not fully unfold even at temperature as high as 150 °C, as shown in Fig. 8(b). This is primarily due to the inability of cellulose-based SLM-FSSs to actuate with temperature and reduction of effective surface temperature of the spacer layer. The proposed polyester-based Miura FSS structure starts to unfold when heated beyond 35 °C in an oven and realizes complete unfolded configuration at 50 °C with an unfolding rate of $\theta = 4°$ per °C.

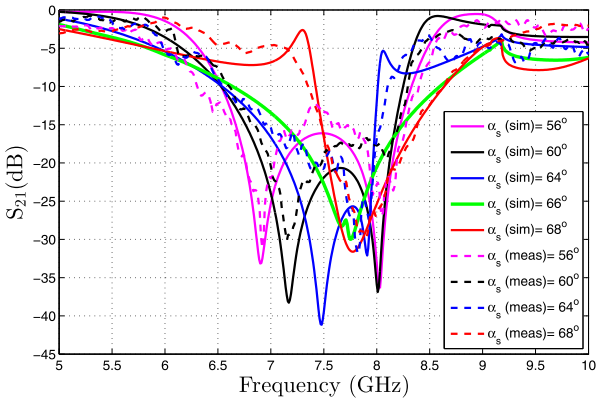

Fig. 9. Frequency response of an MLM-FSS structure ($\theta = 90°$) for different values of internal angle (α_s) of the spacer layer.

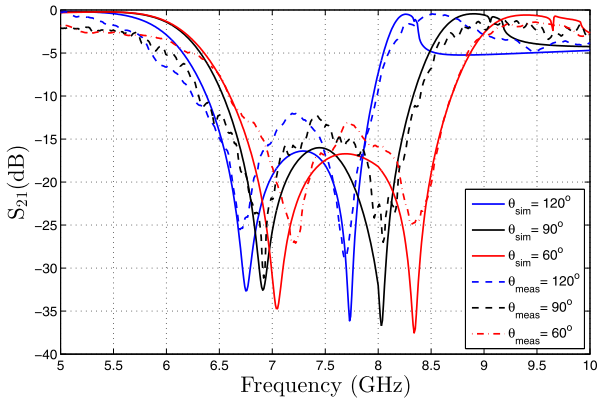

Fig. 10. Frequency response of an MLM-FSS structure ($\alpha_s = 56°$) for different values of folding angle (θ).

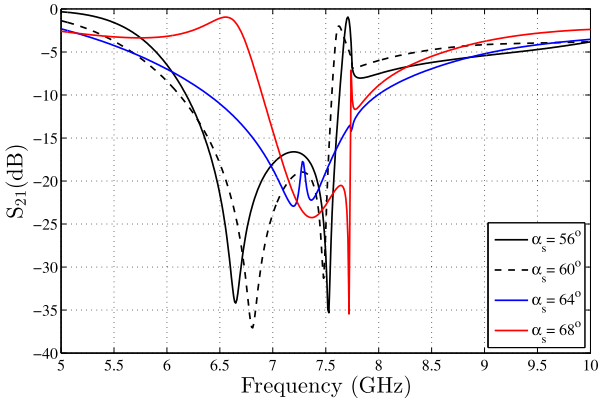

Fig. 11. Frequency response of the MLM-FSS ($\theta = 150°$ and $\alpha_s = 56°$) for different values of AoI.

The proposed MLM-FSS configuration presents a first-of-its-kind integrated actuation mechanism that can be programmed to maintain a given frequency response as well as features higher mechanical strength as compared with SLM-FSS despite its low thickness [19], thus making it an attractive candidate for rugged environment and sandwich structures that have recently found many applications in aerospace, civil, and mechanical engineering [13].

IV. Simulation and Measurement Results

The unit cell of the proposed MLM-FSS was simulated using master/slave boundary conditions in high frequency structure simulator (HFSS) with Floquet port excitation. The simulated results were then verified by using two broadband horn antennas in line-of-sight to each other with the MLM-FSS in the middle. Specialized 3-D printed frames were used to hold the MLM-FSS structure at $\theta = 60°, 90°$, and $120°$. However, these frames would not be required for practical applications, as θ can be increased by simple temperature variation. It is important to note that since the substrate thickness is very low as compared to the wavelength of the desired operational frequency range used in this article, the effects of dielectric losses can be ignored [1]. Moreover, the polyester-based substrate features relatively similar dielectric properties compared with cellulose substrates ($\epsilon_r = 2.47$ and $\tan\delta = 0.07$ at 8 GHz); thus, the frequency response of the proposed MLM-FSS structure would closely resemble that of cellulose-based MLM-FSS structure presented in [19].

The simulated and measured insertion loss (S_{21}) of the MLM-FSS with respect to different values of α_s is shown in Fig. 9, which clearly indicates that at lower values of α_s, the structure exhibits broadband behavior with two distinct resonances. The lower resonance frequency is the result of the mutual coupling between the two SLM-FSS layers, while the higher frequency is the resonant frequency of the individual SLM-FSS layers. The interlayer distance increases with α_s, which results in shifting the coupling frequency toward the resonant frequency value. This behavior can also be predicted by using Fig. 4. For example, an SLM-FSS structure resonates at 7.75 GHz for folding angle $\theta = 90°$ (equivalent wavelength $\lambda = 38.6$ mm) [10]. Using Fig. 4, we can see that in order to realize interlayer spacing ($\Delta h = \lambda/2 = 19.3$ mm), $\alpha_s \approx 66°$. This would ensure a strong coupling between the two SLM-FSS layers resulting in a single wideband resonance (bandstop) filter response of the MLM-FSS structure, as shown in Fig. 9. Beyond this point, the interlayer distance increases more than half of the operational frequency wavelength, resulting in weaker coupling between the two SLM-FSS layers. The slight mismatch between the experimental and theoretical results is caused by the finite size of the sample, which introduces surface currents on the structure [28]. While this problem can be easily solved by increasing the sample size, in this article, the sample size is limited by the total printing limit of the inkjet printer.

Similarly, it is interesting to note here that not only the frequency response of the proposed MLM-FSS systematically shifts to higher frequency, but its frequency response is also preserved with variation in θ, as shown in Fig. 10. This clearly shows that the proposed spacer varies the interlayer distance proportionally with respect to shift in the resonant frequency of the two SLM-FSS layers as they were folded. This condition is true for any given α_s as long as $\Delta h \leq D_l/2$ for $l_c \sim a$, where l_c is the length of dipole. Note that in this case, $D_l/2 = l/2$ represents the effective length of the dipole. For example, the frequency response of the proposed MLM-FSS for different values of α_s with $\theta = 150°$ is shown in Fig. 11, which clearly shows that for $\alpha_s < 64°$, the MLM-FSS preserves its multiresonant filtering response.

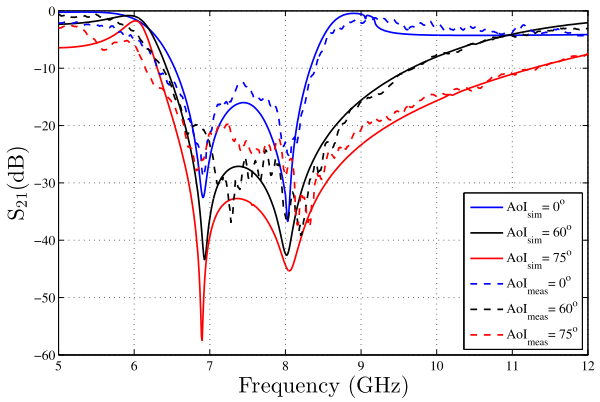

Fig. 12. Frequency response of the MLM-FSS ($\theta = 90°$ and $\alpha_s = 56°$) for different values of AoI.

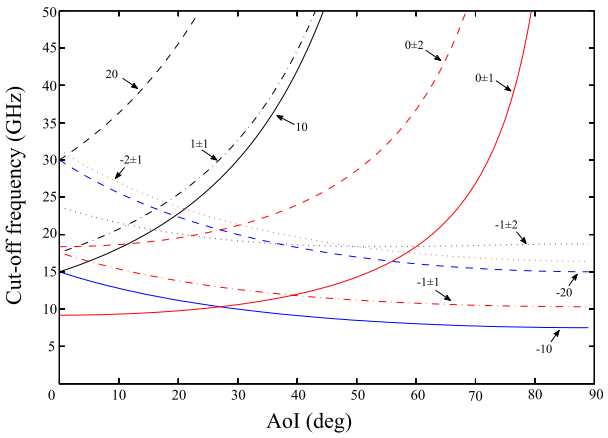

Fig. 13. Cutoff frequencies associated with higher order TE mnth harmonics excited in the proposed MLM-FSS as a function of AoI.

However, the interelement spacing condition is violated for higher values of α_s (as shown in Fig. 4), and hence, they exhibit different EM filtering responses at various values of folding angle θ.

The proposed structure facilitates bandwidth up to 24%, which is more than twice the bandwidth of the equivalent SLM-FSS; however, the tunability range is comparable, which can be increased by using ripple-Miura FSS [12]. The sudden null after the second resonant frequency in the frequency response indicates the onset of grating lobes, which also changes with θ, and thus, no unwanted diffraction effects take place as the structure is tuned to higher frequencies [1]. Finally, the proposed MLM-FSS features a very wide-angle angle of incidence (AoI) rejection (up to 75°) without any shift in any of the two resonant frequencies, as shown in Fig. 12. The increase in the bandwidth is an inherent feature of the dipole FSS, which increases as 1/cos (AoI) for different values of AoI scanned in the H-plane (TE mode) [1].

A. Grating Lobe Behavior

Typically, FSSs are designed to operate in the *no grating lobe* region, where the incident EM wave is reflected or transmitted in the direction depicted by Snell's law. Therefore, it is important to know the cutoff frequency for the onset of grating lobes or trapped modes [1], [29]. For a free standing FSS, the cutoff frequency of the first high-order Floquet mode occurs at [30]

$$f_c^{\epsilon_r} = \frac{c}{D_l(\sqrt{\epsilon_r} + \sin(\text{AoI}))} \tag{4}$$

where c is the speed of light, and ϵ_r is the relative permittivity of the medium where FSS is embedded. For frequencies lower than f_c, the only propagating Floquet harmonic is the fundamental one and higher order modes are considered to be evanescent that decay exponentially moving away from the FSS structures. The onset of higher order modes is essential for accurately depicting the ECM of a given FSS beyond the grating-lobe region [30]. In the case of dipole-based Miura-FSS structures, the cutoff frequencies of higher order TE modes can be determined by taking advantage of the periodic nature of the FSS structure and defining wavenumbers in the x- and y-axes associated with the space harmonics as [1] and [31]

$$k_{x,m} = k_0 \sin\theta + \frac{2\pi m}{D_w} \tag{5}$$

$$k_{x,m} = \frac{2\pi n}{D_l} \tag{6}$$

where $m, n = 0, \pm1, \pm2, \ldots$ and $k_0 = 2\pi f/c$ is the free-space wavenumber. Each higher order Floquet harmonic is defined by a pair of integers mn with the complex wavenumber along the z-axis [31]

$$k_{z,mn}^{\epsilon_r} = \begin{cases} \beta_{mn} = \sqrt{k_0^2\epsilon_r - k_{x,m}^2 - k_{y,n}^2}, & f \geq f_{c,mn}^{\epsilon_r} \\ -j\alpha_{mn} = -j\sqrt{k_{x,m}^2 + k_{y,n}^2 - k_0^2\epsilon_r}, & f < f_{c,mn}^{\epsilon_r} \end{cases} \tag{7}$$

where $f_{c,mn}^{\epsilon_r}$ is the cutoff frequency of the mnth harmonic that satisfies

$$\gamma_{mn}^2 = k_{x,m}^2 + k_{y,n}^2 - k_0^2\epsilon_r = 0 \tag{8}$$

and can be expressed as

$$f_{c,mn}^{\epsilon_r} = \frac{\chi}{\epsilon_r - \sin^2(\text{AoI})} \tag{9}$$

where

$$\chi = \frac{mc\sin(\text{AoI})}{D_w} + \sqrt{\epsilon_r\left[\left(\frac{mc}{D_w}\right)^2 + \left(\frac{nc}{D_l}\right)^2\right] - \frac{nc\sin(\text{AoI})^2}{D_l}}.$$

Note that for normal incidence (AoI = 0°), (9) reduces to the expression for the cut-off frequency of rectangular waveguide with dimensions D_l and D_w. The cutoff frequencies that are associated with the higher order TE mnth harmonics excited in the proposed MLM-FSS structure as a function of AoI are shown in Fig. 13.

The sudden null in the frequency response of the MLM-FSS structure after the main resonance(s) depicts the excitation of higher order mode (TE_{10}) and the onset of grating lobes; therefore, it is necessary to understand its behavior with respect

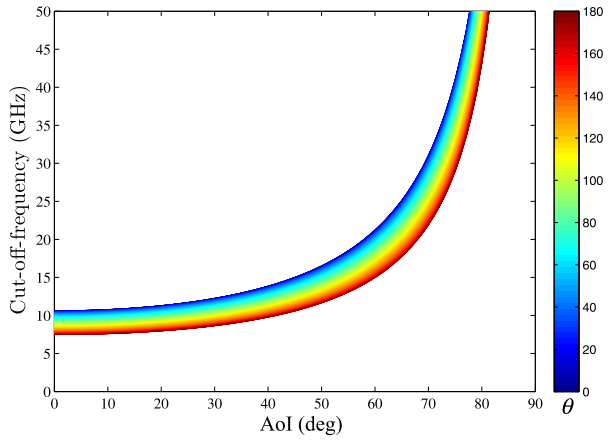

Fig. 14. Cutoff frequency of grating lobes for the different values of AoI and θ ($\alpha_s = 56°$ and $\alpha_p = 45°$).

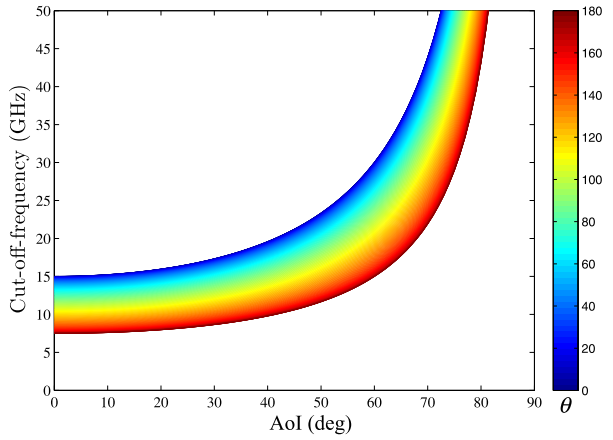

Fig. 15. Cutoff frequency of grating lobes for different values of AoI and θ ($\alpha_s = 56°$ and $\alpha_p = 60°$).

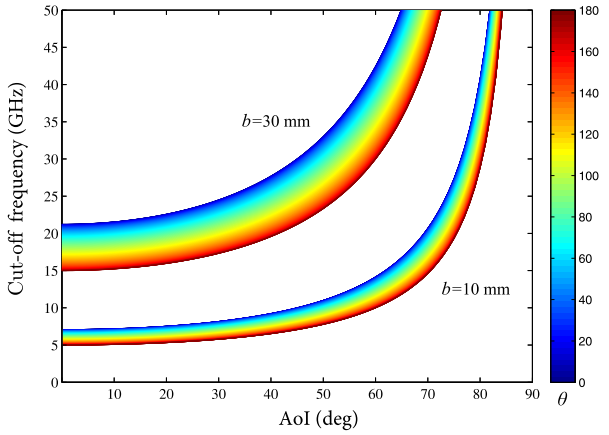

Fig. 16. Cutoff frequency of grating lobes for the different values of AoI, θ, and b ($\alpha_s = 56°$ and $\alpha_p = 45°$).

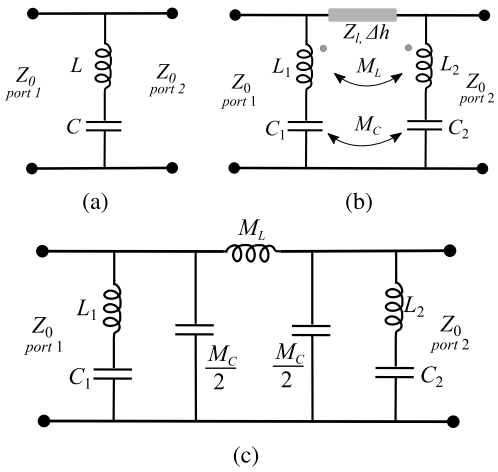

Fig. 17. Equivalent circuit of (a) SLM-FSS and MLM-FSS with spacer represented by (b) transmission line model and (c) lumped-element model.

to different design parameters of the MLM-FSS structure. The variation of grating lobe cut off frequency with respect to α_p, θ, and AoI is shown in Figs. 14 and 15, which clearly show that the grating-lobe cutoff frequency shifts to higher values much slower, as the MLM-FSS structure is folded (θ is varied) for small α_p although the shift is more pronounced for higher values of α_p. This trend is also true for the design parameter b, as shown in Fig. 16. Note that as expected, the grating-lobe region can be effectively moved to higher frequency ranges by simply increasing the interelement distances using b or α_p.

B. ECM

The EM behavior of the MLM-FSS can be approximated using the ECM, where each SLM-FSS layer with dipole elements can be represented by a series LC network connected across two ports with intrinsic impedance ($Z_o = 377\ \Omega$), as shown in Fig. 17(c)—the first-order bandstop filter. The corresponding values of the inductance (L) and capacitance (C) are dictated by dipole length and their interelement distances, respectively [1]. Since the thickness of the polyester-based substrate is much smaller than the operational frequency range of the proposed MLM-FSS structures, the dielectric effects were not included in this model for simplicity [1].

Similarly, the equivalent circuit of the proposed MLM-FSS is shown in Fig. 17(b), where the values of L_n and C_n (where $n = 1, 2$) were determined by the two resonant frequencies and the spacer is represented by a transmission line, whose electrical length (l) depends on thickness of the spacer (or equivalently Δh) [32]. The characteristic impedance of the spacer is $Z_l = Z_o/\sqrt{\epsilon_r}$, where ϵ_r and Z_o are the relative permittivity of spacer and the characteristic impedance of free space, respectively. However, the dielectric effects of the spacer can be ignored in this case, as the effective permittivity of the spacer is almost equal to that of free space (ϵ_o) [1]. Hence, the equivalent model of the proposed Miura-FSS can be reduced to two series LC networks connected across the two ports [with ($Z_o = 377\ \Omega$)], where the mutual inductance and capacitance between the layers are represented by M_L and M_C, respectively. The numerical values of L_n and C_n can be determined by the following procedure.

1) Determine the resonant frequencies of the MLM-FSS (f_1 and f_2) using a full-wave simulator, where each

TABLE I

CAPACITANCE AND INDUCTANCE VALUES OF PROPOSED MLM-FSS ECM FOR VARIOUS VALUES OF α_s ($\theta = 90°$)

α_s	f_1 (GHz)	L_1 (nH)	f_2 (GHz)	L_2 (nH)	Δh (mm)
54°	8	18.04	6.9	13.54	6.82
60°	8	18.04	7.15	10.84	10.35
64°	8	18.04	7.5	9.94	14.85
68°	7.8	18.04	7.8	7.24	20.86

TABLE II

CAPACITANCE AND INDUCTANCE VALUES OF THE PROPOSED MLM-FSS ECM (WITH $\alpha_s = 56°$) FOR VARIOUS VALUES OF FOLDING ANGLE θ

θ	f_1 (GHz)	L_1 (nH)	f_2 (GHz)	L_2 (nH)	Δh (mm)
120°	7.75	32.4	6.75	10.84	7.14
90°	8	18.04	6.9	13.54	10.35
60°	8.4	14.4	7.1	16.84	5.62

resonant frequency can be represented by

$$\omega_r = \frac{1}{\sqrt{LC}}. \tag{10}$$

Then, using (10), assign $C_n = 1/(L_n 2\pi f_n)^2$, where L_n is kept variable. This would ensure that the ECM has the same resonant frequency as the full-wave simulation and only differs in bandwidth. Note that in this case, the initial value of L_n becomes irrelevant.

2) Set the electrical length of the transmission line according to Δh.
3) Choose two frequency points on the S_{21} plot of the MLM-FSS structure. In this article, the frequency points at $S_{21} = -10$ dB were chosen.
4) Iteratively vary the values of L_n such that the overall equivalent-circuit response has the minimum Euclidean distance from the full-wave simulation.

Note that for single resonance broadband case ($\alpha_s > 66°$), $L_1 = L_2$ and $C_1 = C_2$. Moreover, the effect of the transmission line can also be translated to equivalent π-LC network, as shown in Fig. 17(b), where the mutual coupling coefficients can be calculated using (11) and (12) [33]

$$M_L = \mu_o \mu_r \Delta h \tag{11}$$

$$M_C = \frac{\epsilon_o \epsilon_r \Delta h}{2} \tag{12}$$

where ω_r is the resonant frequency of the SLM-FSS, and μ_o and μ_r are the permeability of free space and the relative permeability of the spacer, respectively. The transmission-line approach is used in this article since it is more intuitive and can be easily extended to MLM-FSS structures with more than two SLM-FSS layers. The capacitance and inductance values of the proposed MLM-FSS ECM for different values of interlayer distances (α_s) and folding angle (θ) are given in Tables I and II, respectively. In order to validate the ECM, frequency response of the MLM-FSS (with $\alpha_s = 56°$, $\alpha_p = 45°$, and $\theta = 90°$) is evaluated and compared with the HFSS, as shown in Fig. 18. The sudden null in the frequency response of the MLM-FSS structure represents the onset of the grating lobes. The proposed ECM assumes that FSS operates in the *no grating lobe* region that is why the effect of grating lobes is not included. However, this can be easily accounted for by using the procedure outlined in [34] and [35].

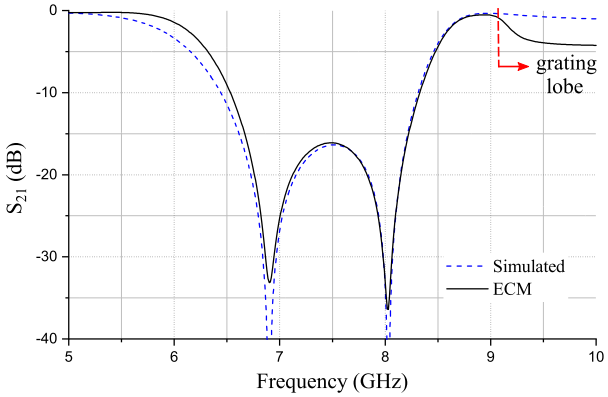

Fig. 18. MLM-FSS frequency response comparison between HFSS simulation and ECM.

V. CONCLUSION

This article presents a state-of-the-art fully inkjet-printed MLM-FSS structure with dipole resonant elements and a specialized origami-inspired shape reconfigurable spacer layer. Proposed MLM-FSS structure is realized using a thermal-sensitive polyester-based substrate that can transform its physical shape from a completely folded to fully unfolded configuration based on the change in its ambient temperature. It addresses some of the major drawbacks of the previously reported SLM-FSS structures, including narrowband frequency response, poor mechanical stability, and use of mechanical actuation mechanism, making them unsuitable for applications with limited available power. The smart shape-shifting spacer is the first demonstration of its kind, which preserves the in-plane kinematics and proportionally varies the interlayer distances between MLM FSS structures for every folding configuration, thereby maintaining the desired frequency response of the filter. Bandwidth of the proposed structure is more than double as compared to the SLM-FSS and can be varied by simply changing the design parameters of the spacer layer. It also facilitates perfect alignment of the Miura-FSS structure for an in-line stacking configuration to mitigate any misalignment errors that may occur during the assembly. A detailed analysis of the MLM-FSS frequency response with respect to change in folding angle (θ), AoI, and interlayer distances along with its relationship with the Miura kinematics is presented in this article. EM behavior of the structure is also explained in terms of the ECM. The simulation results show strong agreement with the measurement results. Proposed MLM-FSS structure truly represents the uniqueness and substantial advantage of additive manufacturing technologies and origami-inspired RF structures since such structures would be impossible to realize using traditional manufacturing technologies. Moreover, these design principles can be extended to realize higher order tunable FSS structures without loss of generality, giving the designer an unprecedented freedom to design custom-based FSS structure suitable for a given application.

REFERENCES

[1] B. A. Munk, *Frequency Selective Surfaces: Theory and Design*. Hoboken, NJ, USA: Wiley, 2000.

[2] T. K. Wu, *Frequency Selective Surface and Grid Array* (Wiley Series in Microwave and Optical Engineering). Hoboken, NJ, USA: Wiley, 1995.

[3] Y. J. Sung, T. U. Jang, and Y. S. Kim, "A reconfigurable microstrip antenna for switchable polarization," *IEEE Microw. Wireless Compon. Lett.*, vol. 14, no. 11, pp. 534–536, Nov. 2004.

[4] S. Nikolaou *et al.*, "Pattern and frequency reconfigurable annular slot antenna using PIN diodes," *IEEE Trans. Antennas Propag.*, vol. 54, no. 2, pp. 439–448, Feb. 2006.

[5] C. W. Jung, M.-J. Lee, G. P. Li, and F. De Flaviis, "Reconfigurable scan-beam single-arm spiral antenna integrated with RF-MEMS switches," *IEEE Trans. Antennas Propag.*, vol. 54, no. 2, pp. 455–463, Feb. 2006.

[6] C. R. White and G. M. Rebeiz, "Single- and dual-polarized tunable slot-ring antennas," *IEEE Trans. Antennas Propag.*, vol. 57, no. 1, pp. 19–26, Jan. 2009.

[7] F. Bayatpur and K. Sarabandi, "Design and analysis of a tunable miniaturized-element frequency-selective surface without bias network," *IEEE Trans. Antennas Propag.*, vol. 58, no. 4, pp. 1214–1219, Apr. 2010.

[8] T. K. Chang, R. J. Langley, and E. A. Parker, "Frequency selective surfaces on biased ferrite substrates," *Electron. Lett.*, vol. 30, no. 15, pp. 1193–1194, Jul. 1994.

[9] M. Li and N. Behdad, "Fluidically tunable frequency selective/phase shifting surfaces for high-power microwave applications," *IEEE Trans. Antennas Propag.*, vol. 60, no. 6, pp. 2748–2759, Jun. 2012.

[10] S. A. Nauroze, L. Novelino, M. M. Tentzeris, and G. H. Paulino, "Inkjet-printed '4D' tunable spatial filters using on-demand foldable surfaces," in *IEEE MTT-S Int. Microw. Symp. Dig.*, Jun. 2017, pp. 1575–1578.

[11] K. Fuchi, J. Tang, B. Crowgey, A. R. Diaz, E. J. Rothwell, and R. O. Ouedraogo, "Origami tunable frequency selective surfaces," *IEEE Antennas Wireless Propag. Lett.*, vol. 11, pp. 473–475, 2012.

[12] S. A. Nauroze, A. Eid, and M. M. Tentzeris, "n-RiM: A paradigm shift in the realization of fully inkjet-printed broadband tunable FSS using origami structures," in *IEEE MTT-S Int. Microw. Symp. Dig.*, Jun. 2018, pp. 51–54.

[13] Y. Klett, P. Middendorf, W. Sobek, W. Haase, and M. Heidingsfeld, "Potential of origami-based shell elements as next-generation envelope components," in *Proc. IEEE Int. Conf. Adv. Intell. Mechatronics (AIM)*, Jul. 2017, pp. 916–920.

[14] M. Arya, J. F. Sauder, R. Hodges, and S. Pellegrino, "Large-area deployable reflectarray antenna for CubeSats," in *Proc. AIAA Scitech Forum*, 2019, p. 2257.

[15] S. A. Nauroze, L. S. Novelino, M. M. Tentzeris, and G. H. Paulino, "Continuous-range tunable multilayer frequency-selective surfaces using origami and inkjet printing," *Proc. Nat. Acad. Sci. USA*, vol. 115, no. 52, pp. 13210–13215, 2018.

[16] S. I. H. Shah, D. Lee, M. M. Tentzeris, and S. Lim, "A novel high-gain tetrahedron origami," *IEEE Antennas Wireless Propag. Lett.*, vol. 16, pp. 848–851, 2016.

[17] W. Saad, M. Bennis, and M. Chen, "A vision of 6G wireless systems: Applications, trends, technologies, and open research problems," 2019, *arXiv:1902.10265*. [Online]. Available: https://arxiv.org/abs/1902.10265

[18] L. Subrt and P. Pechac, "Controlling propagation environments using intelligent walls," in *Proc. 6th Eur. Conf. Antennas Propag. (EUCAP)*, Mar. 2012, pp. 1–5.

[19] S. A. Nauroze and M. M. Tentzeris, "Fully inkjet-printed multilayer tunable origami FSS structures with integrated thermal actuation mechanism," in *IEEE MTT-S Int. Microw. Symp. Dig.*, Jun. 2019, pp. 1363–1366.

[20] S. A. Nauroze, J. Hester, W. Su, and M. M. Tentzeris, "Inkjet-printed substrate integrated waveguides (SIW) with 'drill-less' vias on paper substrates," in *IEEE MTT-S Int. Microw. Symp. Dig.*, May 2016, pp. 1–4.

[21] M. R. Ayatollahi, S. M. J. Razavi, and H. R. Chamani, "Fatigue life extension by crack repair using stop-hole technique under pure mode-I and pure mode-II loading conditions," *Procedia Eng.*, vol. 74, no. 74, pp. 18–21, 2014.

[22] S. A. Nauroze *et al.*, "Additively manufactured RF components and modules: Toward empowering the birth of cost-efficient dense and ubiquitous IoT implementations," *Proc. IEEE*, vol. 105, no. 4, pp. 702–722, Apr. 2017.

[23] Y. Cui, S. A. Nauroze, and M. M. Tentzeris, "Novel 3D-printed reconfigurable origami frequency selective surfaces with flexible inkjet-printed conductor traces," in *IEEE MTT-S Int. Microw. Symp. Dig.*, Jun. 2019, pp. 1367–1370.

[24] C. Yuan, T. Wang, M. L. Dunn, and H. J. Qi, "3D printed active origami with complicated folding patterns," *Int. J. Precis. Eng. Manuf.-Green Technol.*, vol. 4, no. 3, pp. 281–289, 2017.

[25] A. Zolfagharian *et al.*, "3D printing of a photo-thermal self-folding actuator," *KnE Eng.*, pp. 15–22, Feb. 2017.

[26] M. Z. Miskin *et al.*, "Graphene-based bimorphs for micron-sized, autonomous origami machines," *Proc. Nat. Acad. Sci. USA*, vol. 115, no. 3, pp. 466–470, Jun. 2018.

[27] H. Okuzaki, T. Saido, H. Suzuki, Y. Hara, and H. Yan, "A biomorphic origami actuator fabricated by folding a conducting paper," *J. Phys., Conf. Ser.*, vol. 127, no. 1, 2008, Art. no. 012001.

[28] B. A. Munk, *Finite Antenna Arrays and FSS*. Hoboken, NJ, USA: Wiley, 2003.

[29] S. Monni, G. Gerini, A. Neto, and A. G. Tijhuis, "Multimode equivalent networks for the design and analysis of frequency selective surfaces," *IEEE Trans. Antennas Propag.*, vol. 55, no. 10, pp. 2824–2835, Oct. 2007.

[30] F. Costa, A. Monorchio, and G. Manara, "An overview of equivalent circuit modeling techniques of frequency selective surfaces and metasurfaces," *Appl. Comput. Electromagn. Soc. J.*, vol. 29, no. 12, pp. 960–976, Dec. 2014.

[31] M. García-Vigueras, F. Mesa, F. Medina, R. Rodríguez-Berral, and J. L. Gómez-Tornero, "Simplified circuit model for arrays of metallic dipoles sandwiched between dielectric slabs under arbitrary incidence," *IEEE Trans. Antennas Propag.*, vol. 60, no. 10, pp. 4637–4649, Oct. 2012.

[32] K. Sarabandi and N. Behdad, "A frequency selective surface with miniaturized elements," *IEEE Trans. Antennas Propag.*, vol. 55, no. 5, pp. 1239–1245, May 2007.

[33] A. Ebrahimi *et al.*, "Second-order terahertz bandpass frequency selective surface with miniaturized elements," *IEEE Trans. THz Sci. Technol.*, vol. 5, no. 5, pp. 761–769, Sep. 2015.

[34] R. Rodríguez-Berral, F. Mesa, F. Medina, and M. García-Vigueras, "Analytical circuit model for dipole frequency-selective surfaces," in *IEEE MTT-S Int. Microw. Symp. Dig.*, Jun. 2013, pp. 1–4.

[35] F. Mesa, R. Rodríguez-Berral, and F. Medina, "Unlocking complexity using the ECA: The equivalent circuit model as an efficient and physically insightful tool for microwave engineering," *IEEE Microw. Mag.*, vol. 19, no. 4, pp. 44–65, Jun. 2018.

Syed Abdullah Nauroze (S'13) received the B.Sc. degree (Hons.) in computer engineering from the University of Engineering and Technology, Taxila, Pakistan, in 2005, and the M.Sc. degree in electrical engineering from the KTH Royal Institute of Technology, Stockholm, Sweden, in 2008. He is currently pursuing the Ph.D. degree in electrical and computer engineering at the Georgia Institute of Technology, Atlanta, GA, USA.

From 2008 to 2009, he was with the Microsystems Technology Laboratory, KTH Royal Institute of Technology, where he conducted research on on-chip millimeter-wave antennas for automotive radar and future wireless applications. He has a teaching experience of seven years. He is currently a Research Assistant with the ATHENA Lab, Georgia Institute of Technology. His current research interests include the application of additive manufacturing techniques such as 3-D printing and ink-jet printing for flexible and origami-based RF structures.

Dr. Nauroze was a recipient of the Prestigious Swedish Institute Scholarship in 2006 and the Fulbright Scholarship in 2014 for his master's and Ph.D. degrees, respectively.

Manos M. Tentzeris (S'89–M'92–SM'03–F'10) received the Diploma degree *(magna cum laude)* in electrical and computer engineering (ECE) from the National Technical University of Athens, Athens, Greece, in 1992, and the M.S. and Ph.D. degrees in electrical engineering and computer science from the University of Michigan, Ann Arbor, MI, USA, in 1993 and 1998, respectively.

He was a Visiting Professor with the Technical University of Munich, Munich, Germany, in Summer 2002, a Visiting Professor with the Georgia Tech Research Institute (GTRI), Athlone, Ireland, in Summer 2009, and a Visiting Professor with the Laboratory for Analysis and Architecture of Systems (LAAS)-CNRS, Toulouse, France, in Summer 2010. He is currently a Professor with the School of ECE, Georgia Tech, Atlanta, GA, USA. He has authored over 550 articles in refereed journals and conference proceedings, five books, and 23 book chapters.

Dr. Tentzeris is a member of the URSI-Commission D, the MTT-15 Committee, and the Technical Chamber of Greece. He is an Associate Member of EuMA and a Fellow of the Electromagnetic Academy. He was a recipient/co-recipient of the 2015 IET Microwaves, Antennas, and Propagation Premium Award, the 2014 Georgia Tech ECE Distinguished Faculty Achievement Award, the 2014 IEEE Radio Frequency Identification Technology and Advancement (RFID-TA) Best Student Paper Award, the 2013 IET Microwaves, Antennas and Propagation Premium Award, the 2012 FiDiPro Award in Finland, the iCMG Architecture Award of Excellence, the 2010 IEEE Antennas and Propagation Society Piergiorgio L. E. Uslenghi Letters Prize Paper Award, the 2011 International Workshop on Structural Health Monitoring Best Student Paper Award, the 2010 Georgia Tech Senior Faculty Outstanding Undergraduate Research Mentor Award, the 2009 IEEE Transactions on Components and Packaging Technologies Best Paper Award, the 2009 E.T.S. Walton Award from the Irish Science Foundation, the 2007 IEEE APS Symposium Best Student Paper Award, the 2007 IEEE IMS Third Best Student Paper Award, the 2007 ISAP 2007 Poster Presentation Award, the 2006 IEEE MTT Outstanding Young Engineer Award, the 2006 Asian-Pacific Microwave Conference Award, the 2004 IEEE TRANSACTIONS ON ADVANCED PACKAGING Commendable Paper Award, the 2003 NASA Godfrey "Art" Anzic Collaborative Distinguished Publication Award, the 2003 IBC International Educator of the Year Award, the 2003 IEEE CPMT Outstanding Young Engineer Award, the 2002 International Conference on Microwave and Millimeter-Wave Technology Best Paper Award, Beijing, China, the 2002 Georgia Tech-ECE Outstanding Junior Faculty Award, the 2001 ACES Conference Best Paper Award, and the 2000 NSF CAREER Award and the 1997 Best Paper Award from the International Hybrid Microelectronics and Packaging Society. He was the TPC Chair of the IEEE IMS 2008 Symposium and the Chair of the 2005 IEEE CEM-TD Workshop. He is the Vice-Chair of the RF Technical Committee (TC16) of the IEEE CPMT Society. He is the Founder and the Chair of the RFID Technical Committee (TC24) of the IEEE MTT Society and the Secretary/Treasurer of the IEEE C-RFID. He has helped to develop academic programs in highly integrated/multilayer packaging for RF and wireless applications using ceramic and organic flexible materials, article-based RFID's and sensors, biosensors, wearable electronics, 3-D/4-D/inkjet-printed electronics, "Green" electronics, energy harvesting and wireless power transfer systems, NFC systems, nanotechnology applications in RF, origami-folded electromagnetics, microwave MEMs, and SOP-integrated (UWB, multiband, mmW, and conformal) antennas and the Head of the ATHENA Research Group (20 researchers). He has served as the Head of the GT-ECE Electromagnetics Technical Interest Group, the Georgia Electronic Design Center Associate Director for RFID/sensors' research from 2006 to 2010, and the Georgia Tech NSF-Packaging Research Center Associate Director for RF Research and the RF Alliance Leader from 2003 to 2006. He is the Associate Editor of the IEEE TRANSACTIONS ON MICROWAVE THEORY AND TECHNIQUES, the IEEE TRANSACTIONS ON ADVANCED PACKAGING, and the *International Journal on Antennas and Propagation*. He has given more than 100 invited talks to various universities and companies all over the world. He served as one of the IEEE MTT-S Distinguished Microwave Lecturers from 2010 to 2012 and he is currently serving as the IEEE C-RFID Distinguished Lecturer.